

An Advanced NCRF Linac Concept for a High Energy e^+e^- Linear Collider

K. Bane, T. Barklow, M. Breidenbach, C. Burkhardt, R. Conley, E. Fauve, A. Gold, V. Heloin, Z. Li, E. Nanni, M. Nasr, M. Oriunno, E. Paterson, M. Peskin, T. Raubenheimer, S. Tantawi

SLAC National Accelerator Laboratory

1. Abstract

An advanced Normal Conducting Radio Frequency (NCRF) C-band linear accelerator (linac) structure has been designed for a high gradient, high power e^+e^- linear collider in the TeV class. The structure features internal manifolds for distributing RF power separately to each cell, permitting the full structure geometry to be designed for high shunt impedance and low breakdown. In addition, the structure is cooled directly by liquid nitrogen (LN), further increasing the shunt impedance. A crucial part of the design process has been cost optimization, and based on achieving the DOE-HEP GARD goal for RF power of \$2/peak kW, the linac would be substantially cheaper than current designs.

2. Introduction

The SLAC NCRF linear collider group has developed a pre-conceptual point design for an e^+e^- linear collider with linac energies of the TeV scale. A primary goal of this design is to understand the impact of recent and future developments and various technology choices which fall in line with the DOE HEP General Accelerator R&D (GARD) RF decadal roadmap. Achieving these advances will provide a transformative impact on the design and operation of future accelerators, opening up new paths for discovery. For this point design, the effort is limited to the accelerator proper and assumes that one can use existing ILC designs and costs both for the required injector systems which include sources, booster linacs, damping rings, bunch-length compressors, and for outfitting tunnels.¹ These injector systems have been studied for a wide variety of linear collider parameters. Although the details are affected by the choice for the main accelerator RF frequency, the bunch train patterns, and the repetition rate, the injector systems for the different configurations have much in common. The damping rings are the largest of the sub-systems in size and cost. All rings have wiggler dominated designs at a few GeV beam energy and with a circumferences of a few kilometers in order to handle the large number of bunches per second required to achieve the desired luminosity. The ILC injector systems are typical and can be assumed as generic for these studies where the main accelerator linac is composed of C-band NCRF standing wave structures. For the accelerating structure, we envision a distributed RF topology where each cell is separately fed from a common RF manifold. The accelerator is operated at $\sim 77\text{K}$ in a LN bath to reduce the RF power required to achieve high gradient and also to reduce the break-down rate.² The accelerator optimization depends very strongly on the cost of RF power, and the GARD RF power goals³

are assumed to have been achieved. To guide the design, we scale the accelerator requirements for luminosity and beam power from the existing established CLIC and ILC designs, see Figure 1. Table 1 shows the main parameters for a 2 TeV center of mass (CoM) linac. For lower energy designs, parameters in Table 1 marked with a [†] should scale roughly linearly, with modifications below 300 GeV to maintain a linear luminosity scaling with energy.

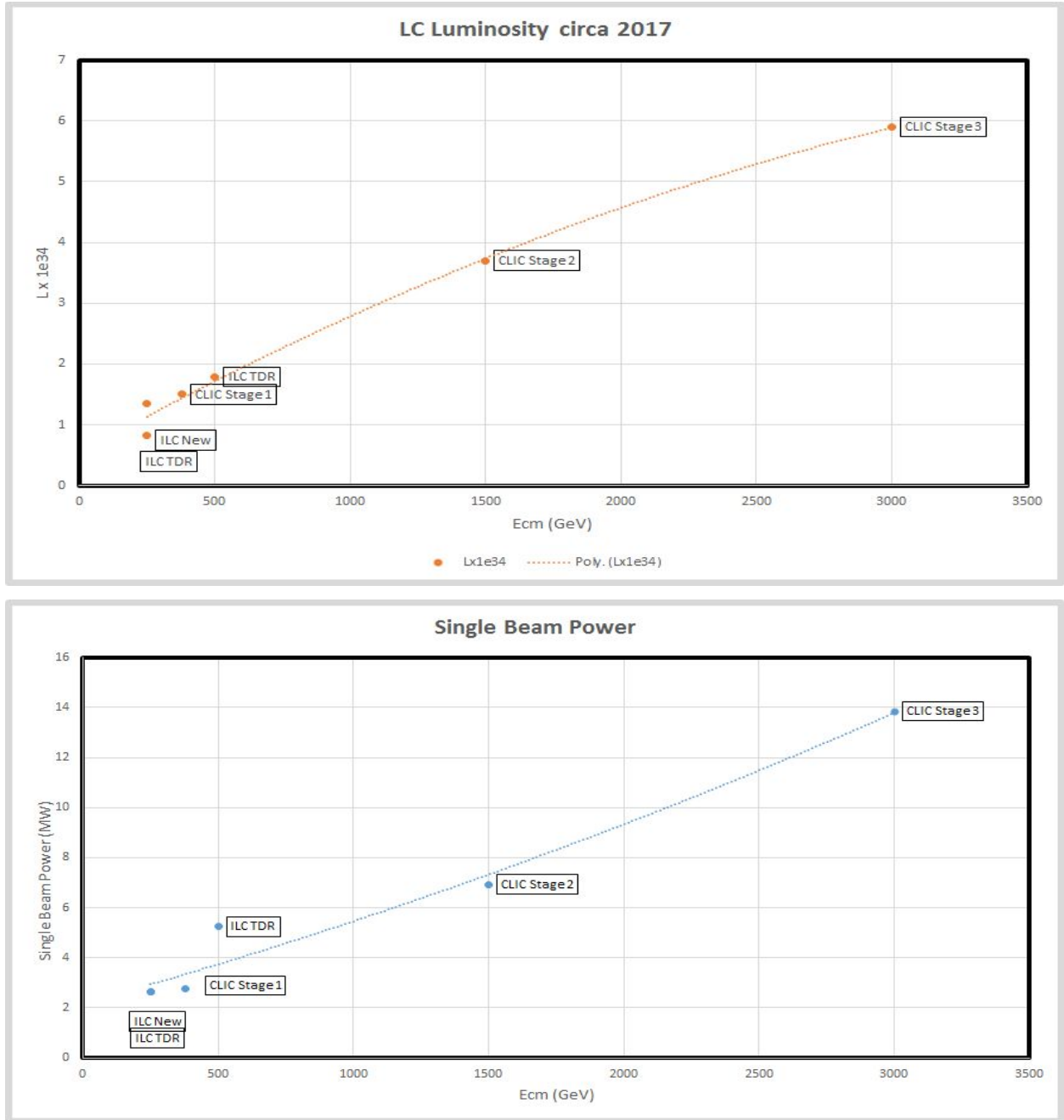


Figure 1 (above) Luminosity and (below) single beam power required as a function of CoM energy⁴.

Parameter	Symbol	Units	Value	Notes
CoM Energy		TeV	2	[†] Denote parameters that scale with CoM Energy
Single Beam Energy [†]	E_b	Gev	1000	
Single Beam Power [†]	P_b	MW	9	
Train Rep Rate		Hz	120	See Figure 2
Bunch Charge	N	$\times 10^{10}$	0.625	1 nC
RF Pulse Length		ns	250	
Bunch Spacing		periods	19	3.3 ns
Average Current		μA	9	
Peak Current		A	0.3	
Luminosity [†]	L	$\times 10^{34} \text{ cm}^{-2}\text{s}^{-1}$	4.5	
Est. AC Power [†]	P_{AC}	MW	250	See Table 4 for subtotals
Est Cooling Power [†]		MW	163	
Operating Temp	T_{op}	K	77	
Linac Gradient		MV/m	117	
Filling Factor			0.9	
Single Linac Length [†]		km	9.5	
Cavity Fundamental		GHz	5.712	
Shunt Impedance		$\text{M}\Omega/\text{m}$	298	
a/λ			0.05	
Beam Loading		Percent	42	

Table 1 Parameters for the Main Linac

3. Physics Case

The results from the LHC give renewed motivation to study e^+e^- annihilation at high energy. First, the LHC experiments have discovered the Higgs boson and measured its mass. This discovery opens the door to the study of this last crucial element of the Standard Model of Particle Physics (SM) and defines the parameters for high-precision measurements of the properties of this particle. Second, the LHC has carried out extensive searches for new particles associated with models of fundamental physics. Thus far, no new particles have been found. Though there is still space to cover before reaching the ultimate limits of the LHC, the window is closing. However, the LHC cannot rule out particles with only electroweak interactions whose signatures at the LHC are subtle and elusive. There are important examples of such particles that are more easily discovered at e^+e^- colliders.

These considerations lead to an important program of experiments to be carried out at future e^+e^- colliders. To provide context, we briefly summarize these experiments in this section. They are now being studied for the physics programs of the ILC and CLIC. It is by no means assured that either of these colliders will go forward, or that whatever next e^+e^- collider is built will reach multi-TeV energies. Still, the full set of experiments listed here should be carried out, and the technology described here may help.

A more complete description of these experiments, their motivation, and projections for achievable sensitivities can be found in the ILC Technical Design Report¹, in the ILC physics updates⁵ and⁶, and in the CLIC Conceptual Design Report⁷. The projections for precision Higgs boson measurements have been updated recently in References ⁸ and ⁹.

a. **Precision measurement of couplings associated with Higgs boson decays:** These are the Higgs boson couplings to W , Z , b , τ , c , μ , γ . It is now understood that measurements at 250 GeV CoM with 2 ab^{-1} and beam polarization (or 5 ab^{-1} without beam polarization) can measure the first three of these couplings in a model-independent way to 1% accuracy or better. The search for deviations from the SM predictions in these couplings gives a new window into physics beyond the SM that is orthogonal to that of particle searches at the LHC. This is a must-do for particle physics. It is important to find an affordable technology and begin this program as soon as possible. Any anomalies discovered in this program could be confirmed by running at 500 GeV CoM or higher, which would add measurements of W fusion production of the Higgs boson. At 500 GeV, the individual coupling errors would be cut in half, and even better results could be expected at higher CoM's, using the cross section for W fusion production of the Higgs boson which rises with increasing CoM.

b. **Search for exotic decays of the Higgs boson:** The Higgs boson may couple to new particles with no SM gauge interactions, including the particle that makes up dark matter.

Measurements at 250 GeV CoM allow comprehensive searches for possible exotic modes of Higgs decay¹⁰.

c. **Precision measurement of the remaining couplings of the Higgs boson:** Two important Higgs boson couplings require higher energy experiments. These are the Higgs coupling to the top quark and the Higgs self-coupling. In both cases, measurements of limited precision can be made at 500 GeV CoM, while higher-precision measurements require even higher energies. At 1 TeV CoM, with 5 ab^{-1} of data, it is possible to measure the htt coupling to 2% accuracy and the hhh coupling to 10%¹¹. The latter analysis uses the complementary processes $e^+e^- \rightarrow Zh h$ and $e^+e^- \rightarrow \nu h h$. It is argued in Reference¹², that, although it is possible to measure double Higgs production in pp collisions, it is very difficult to attribute a deviation from the SM prediction to a shift in the hhh coupling. In fact, it is likely that, for both of these couplings, a precise, model-independent determination is possible only with an e^+e^- collider.

d. **Precision measurement of the top quark mass:** The top quark mass is a fundamental parameter of the SM, and so it is important to measure it as accurately as possible. For most applications, what is needed is a short-distance mass parameter, for example, the \overline{MS} mass. At this moment, it is not understood how to convert the top quark mass quoted by the LHC experiments to a short-distance mass, or even to the top quark pole mass. The conversion from the pole mass to the \overline{MS} mass brings in a perturbative theoretical uncertainty of 200 MeV¹³, plus less well characterized nonperturbative uncertainties. On the other hand, the position of the $t\bar{t}$ threshold in e^+e^- annihilation is controlled by a mass parameter that is very close to the \overline{MS} mass. Measurement of this threshold would give the top quark mass to an accuracy of 40 MeV⁵.

e. **Precision measurement of the top quark electroweak couplings:** Models in which the Higgs boson is composite typically predict sizable deviations from the SM expectations for the W and Z couplings of the top quark. At an e^+e^- collider, the Z vertices appear in the production reaction, where the individual contributions of s -channel γ and Z exchange can be disentangled using beam polarization. This allows measurements of the Z vertices with precisions of better than 1%⁵. These effects are proportional to s/m_Z^2 and so are increasingly visible at higher energies.

f. **Search for pair-production of invisible particles:** Though much attention is being given today to searches for pair-production of invisible particles (including dark matter particles) at the LHC, this is a difficult endeavor. If the dark particles are connected to SM particles by a hard operator or a heavy-mass exchange, it is possible to search for very high pT monojet events. However, if the production is by electroweak Drell-Yan production, the mass reach is limited by QCD and parton distribution uncertainties in the estimation of the irreducible background process, Drell-Yan production of $Z \rightarrow \nu\bar{\nu}$. For example, for Higgsinos, the discovery reach of LHC is expected to be less than 200 GeV¹⁴. In contrast, the pure Higgsino is thermally produced as dark matter with the correct relic density at a mass of about 1 TeV¹⁵.

In e^+e^- annihilation, the corresponding process of photon plus missing momentum is much more precisely understood, allowing searches for invisible particles almost to the kinematic limit¹⁶. Thus, an e^+e^- collider operating above 2 TeV CoM might be the unique way to search for this special dark matter candidate and other high-mass invisible particles.

g. **Search for new electroweak gauge bosons and lepton compositeness:** The processes $e^+e^- \rightarrow f\bar{f}$ can be used to search for new electroweak gauge bosons and for 4-fermion contact interactions including those signalling fermion compositeness. For 3 TeV CoM and 1 ab^{-1} of data, an e^+e^- collider would be sensitive to Z' masses of 15 TeV, more than double the eventual LHC reach. Such a collider would be sensitive to compositeness scales in the range of 60-80 TeV⁷.

Thus, there are strong physics arguments to construct a new, high-energy e^+e^- collider spanning the energy range from 250–350 GeV to multi-TeV CoM.

4. Cost Optimization

The primary obstacle to building any next-generation e^+e^- collider appears to be the cost. The approach of this proposal is therefore to seek the minimum for both capital and operating costs. For an NCRF machine, the dominant capital cost is the RF sources. In practice, an NCRF collider operates with a low duty cycle where the cost of RF sources is driven by the peak power that the RF system must deliver to the linac. RF sources optimized for short pulse and low duty cycle operation can have significantly simplified cooling systems. Other potential simplifications in the design can, for example, reduce susceptibility to oscillations. The GARD RF decadal roadmap specifically lays out these requirements. In particular, it calls for a dramatic improvement in the cost of RF sources (in \$/peak kW) for low duty cycle. The GARD RF power goal is a cost of 2\$/peak kW. We take this as a design assumption for this collider point design and solve for the major parameters of the main linac given in Table 2 through the overall system optimization. The impact of the pulse format on the capital and operating costs is also considered. The repetition rate is kept low at 120 Hz to simplify the cooling of detector electronics and to simplify the damping ring. For the beam format, we have evaluated both individual RF pulses and RF pulse trains repeated at the repetition rate. We found that individual pulses provided reasonable pulse lengths at ~0.25 microseconds. Beam loading has also been optimized to reduce the operational cost of the accelerator, trading increased peak power requirements for higher electrical efficiency and reduced cooling capacity. The temperature of operation (at both 77K and 300K), frequency of operation (C/X-band) and iris aperture were also optimized.

To make the optimization practical, we have assumed conservative values of the outfitted tunnel cost informed by the ILC TDR, and conservative values for the structure cost based on recent SLAC experience. For this point design, we have selected a C-band structure at an operating

temperature of 77K which reduced the overall capital cost of the collider. The pulse format is shown in Figure 2. Single 250 ns RF pulses are repeated at 120 Hz, with 75 x 1 nC electron bunches per pulse at a spacing of 19 periods. The large number of periods separating each bunch aids in suppression of long range wakefields. In this estimate, a 1 TeV linac with 9 MW beam power would cost 3 G\$. For reference, the cost of the linacs in the ILC TDR¹⁷ design (2 x 250 GeV) is estimated at 5200 2012 MILCU. Therefore this is, very roughly, a savings of a factor of 3 per GeV.

Parameter	Units	Value
RF Source Cost	\$/peak kW	2
Temperature	K	77
Main Linac Cost	G\$/TeV	3
Structure Cost	k\$/m	100
Beam Loading	%	42.5
Gradient	MeV/m	117
Pulse Length	ns	250
Cryogenic Load at 77K	MW	27
Electrical Load (two linacs)	MW	250
RF Source efficiency (AC line to linac)	%	50
Train Repetition Rate	Hz	120
Additional linac length (instrumentation, cryogenic feeds, etc)	%	10
Tunnel Cost	k\$/m	50

Table 2 Parameters for 2 x 1 TeV accelerator (excludes final focus, IP, injector, damping ring and pulse compressors)

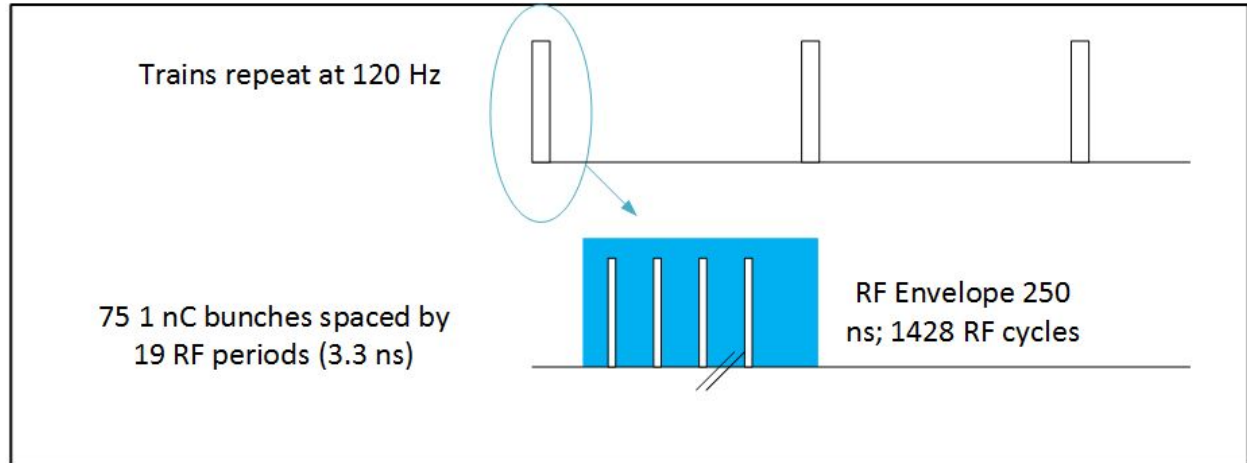


Figure 2 Beam format for the main linac.

5. Cavity Structure

Linear particle accelerators (linacs) accelerate charged particles using oscillating electric fields formed within RF cavities (cells) that are joined together to form a beamline. Charged particles gain energy as they travel along the beamline. Typically, RF power is fed to the linac from one point and flows through adjacent cells using coupling holes that serve also as a beam tunnel for charged particles¹⁸. Consequently, the linac design process requires careful consideration of the coupling between adjacent cells¹⁹. This limits the ability of designers to optimize the cell shape for efficiency and or gradient handling capability.

Distributed coupling linacs²⁰ have a topology that allows feeding each accelerator cell independently using a periodic feeding network. This adds another degree of freedom to the design. The coupling between cells can have a wider acceptable range including almost zero. This allows the geometric optimization of the accelerator cells in order to reach the highest possible shunt impedance or to optimize the field along the cell walls to allow for higher gradient operation²¹.

A distributed coupling accelerator topology is selected for this design in order to maximize the accelerator efficiency and to achieve high gradient. In distributed coupling accelerators, the fundamental accelerating mode of each RF cavity is individually powered and effectively isolated from adjacent cells by a small beam aperture. Each cell can be optimized under fixed constraints, such as peak electric field to accelerating gradient, to maximize the shunt impedance. In addition, the phase advance per cell can also be treated as a free variable. Preliminary studies on single-bunch short range wakefields indicate that for the nominal charge of 1 nC and an operating gradient at or above 100 MeV/m, an iris aperture radius as small as 2.62 mm is tolerable. Harmonic frequencies of 2.856 GHz were investigated for cavity designs. Both C-band and X-band structures achieved similar shunt impedances if the period of the cell was unconstrained. The C-band structure, shown in Figure 3, was selected due to the slightly lower cost of RF power for lower frequencies. Although not the absolute maximum achievable, a

cell period of $\lambda/3$ was selected to simplify the RF distribution manifold required to power the structure. The room temperature and cryogenic shunt impedance of the structure are 133 M Ω /m and 298 M Ω /m, respectively. A summary of the structure parameters is given in Table 4.

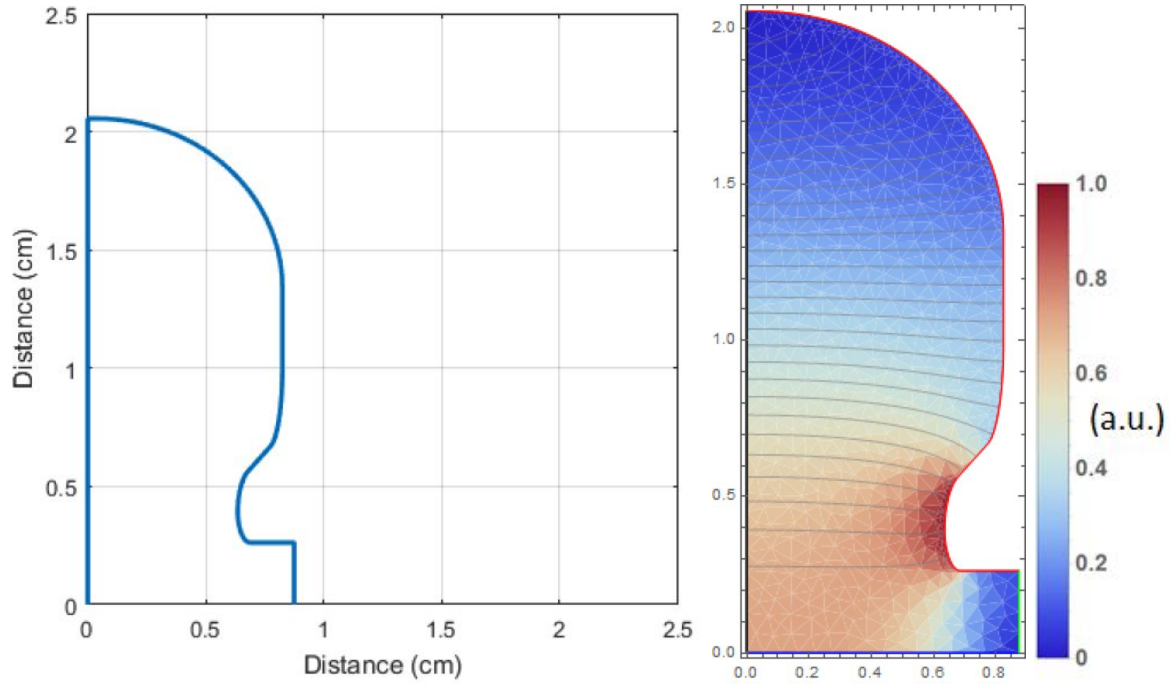


Figure 3 (left) Geometry and (right) electric fields in a C-band cavity of length $\lambda/3$.

At nearly 300 M Ω /m for its planned mode of operation, this structure stands in stark contrast to the structures evaluated for NLC and CLIC even with X-band operation. NLC structures operated with a shunt impedance of up to 98 M Ω /m²² albeit with a larger aperture (3.75 mm). CLIC structures currently under consideration operate with a shunt impedance of 95 M Ω /m.²³ The prospect of a significantly higher shunt impedance dramatically reduces the cost of operation, increases the nominal operating gradient and significantly reduces the peak current required to operate with heavy beam loading. For this point design, the beam loading is 42%. Reducing the peak current also allows a longer bunch spacing of 3.3 ns for 1 nC bunches.

The distributed coupling topology provides additional benefits when operated with heavy beam loading. In particular, the RF distribution manifold powering the cells must be overcoupled to operate efficiently, and this reduces the fill time of the structures. A fill time for the structure equal to or less than the flat top of the gradient or the electron bunch train duration (250 ns) is desirable, as it will help to minimize the additional thermal load. This is possible due to the heavy beam loading of the accelerator which affords us the ability to design highly overcoupled RF coupling to the cavities.

The high shunt impedance also alleviates the requirement for RF pulse compression to achieve the peak power required. Operating at the nominal gradient of 117 MeV/m with 42% beam loading requires only 80 MW of RF power delivered per meter of structure.

Parameter	Units	Value	Notes
Train Rep Rate	Hz	120	See Figure 2
Bunch Charge	$\times 10^{10}$	0.625	1 nC
Bunch Length	μm	100	
Bunch Train Duration	ns	250	
Bunch Spacing	periods	19	3.3 ns
Operating Temp	K	77	
Linac Gradient	MV/m	117	
Cavity Fundamental	GHz	5.712	$\lambda=5.25$ cm
Shunt Impedance	M Ω /m	298	
a/λ		0.05	$a=2.62$ mm
E_{max}/E_a	2.12		
Beam Loading	Percent	42	

Table 3: Structure Parameters

Any concept for a distributed feeding network is required to simultaneously provide power to each cell and the appropriate phase advance for each cell. In this case, the cells are identical and require equal power and a constant phase advance. For a typical electron linac with a particle moving at nearly the speed of light, the phase advance per cell is $2\pi P/\lambda$; where P is the periodic separation between cells and λ is the free space wavelength. With the exception of a dielectric-free coaxial line, this phase advance cannot be provided by any form of wave guiding structure which always has a guided wavelength $\lambda_g > \lambda$.

Alternatively, one can use waveguides oriented so that the center E -plane is the same as the E -plane of the of the accelerator cell.²¹ Because the guided wavelength does not match the free-space wavelength, one can imagine solutions where the distribution waveguide is bent like a serpentine to achieve the appropriate phase advance. This is valid, but one can use more than a single manifold. A natural interval for tapping into the manifold, as shown below, is every $m\lambda_g/2$; where λ_g is the guided wavelength within the manifold, and m is an integer. Therefore, for

a structure with a phase advance/cavity of $2\pi/n$, one can use n manifolds where each one of them is being tapped every λ_g . Hence the phase advance is also an optimization parameter.

A π phase advance/cavity is a special case that simplifies the design of the system. In this case, $n=2$, and hence, only two manifolds are needed. Initial distributed coupling structures, shown in Figure 4, have this mode of operation, which is close to being optimal. For the large-scale optimization of a collider structure with small beam apertures, a phase advance of $2\pi/3$ is slightly better in terms of shunt impedance. An RF distribution manifold will therefore require some serpentine waveguides, Figure 5. As described, each segment of the distributed-coupling accelerator structure can be manufactured from two blocks as shown in Figure 4. The structure is designed so there are no currents crossing the mid-plane along the long dimension. This reduces the complexity of manufacturing the structure and provides logical places for both the cooling manifolds and the tuning holes. The circuit halves are aligned with an elastic averaging technique.

The manifold network consists of a set of cascaded T-junctions. The power going through the tap-off ports to the cavities achieves a minimal standing wave ratio (SWR) with the feeding lines to the cavities. The feeding network, then, has minimal influence on the cavity cells, resulting in two isolated systems (the feeding network and the cavity cells). To this end the cavity coupling port is designed to give a matched port when the cavity is loaded with the design current.

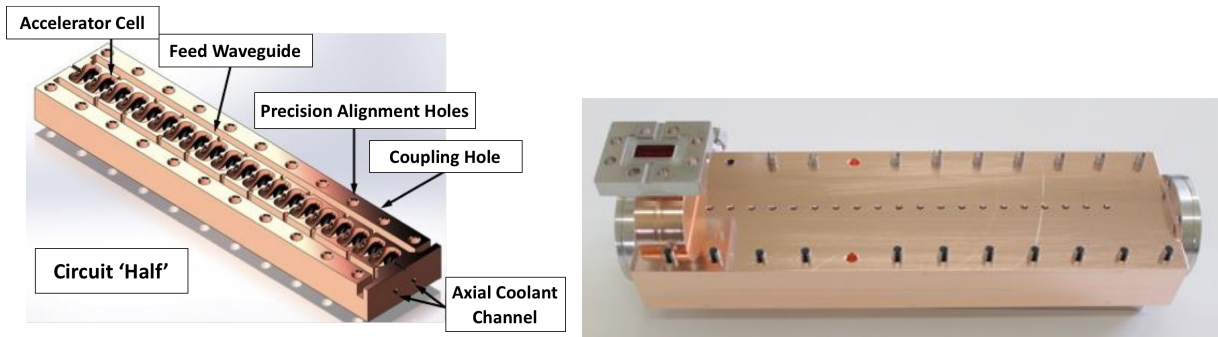


Figure 4 (Left) Illustration and (right) photograph of the distributed coupling linac constructed from two quasi-identical copper blocks, including the tuning pins, alignment holes and cooling channels.

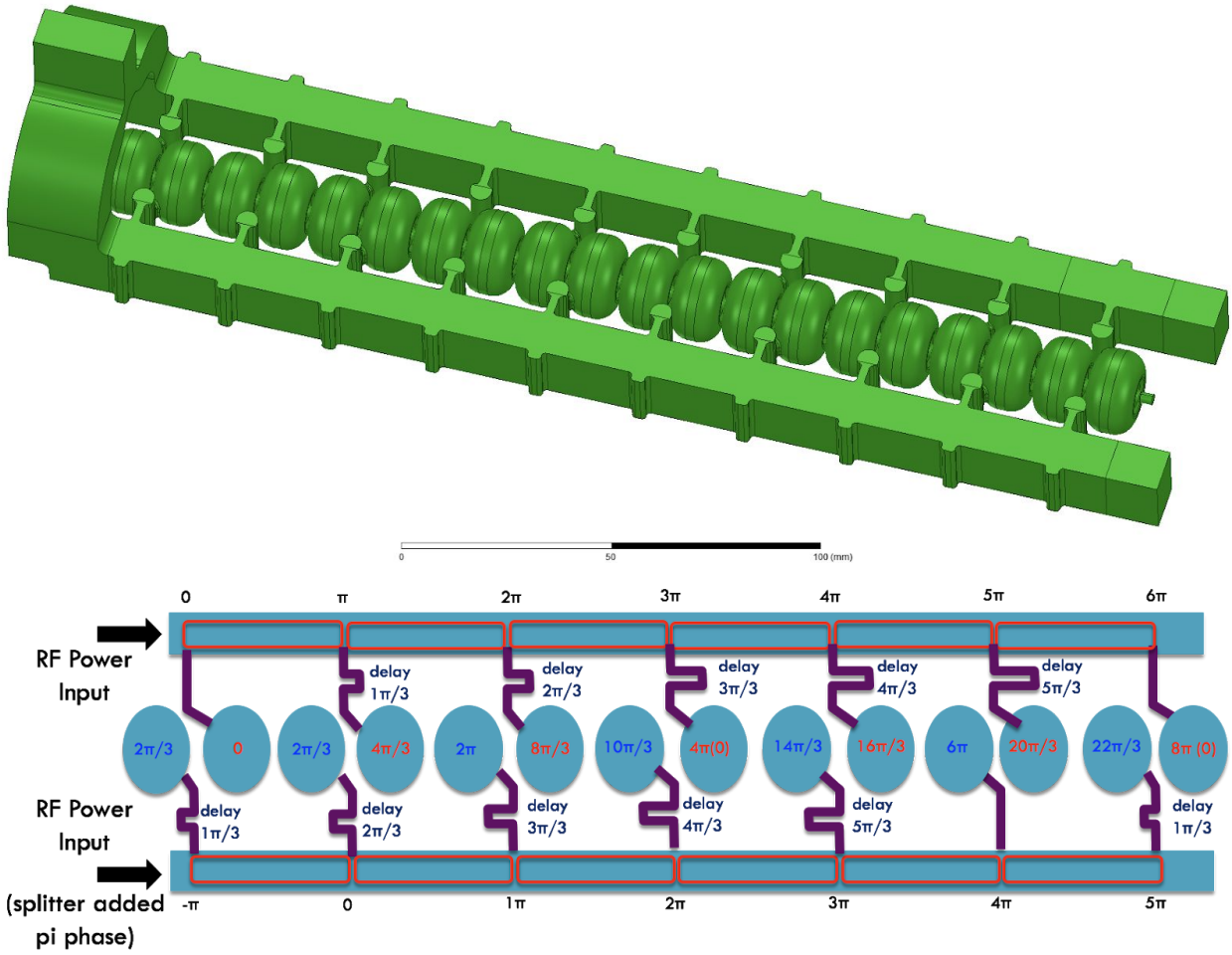


Figure 5 (top) Solid model of the vacuum space for the RF manifold and cavities of an X-band π phase advance structure. (bottom) Schematic of the serpentine RF distribution for the proposed parallel feed waveguide $2\pi/3$ C-band structure.

6. Wakefields

Wakefields and the resulting emittance degradation are of significant concern for any practical collider design. A complete wakefield analysis requires advanced beam dynamics simulations that account for both short-range and long-range effects. They must include operational machine tolerances, the design and optimization of wakefield damping and cell detuning to mitigate long-range wakes. While a complete analysis and design is beyond the scope of this work, an initial effort to ascertain the validity of this structure was undertaken using the performance characteristics of existing collider designs.

a. Short-Range Wakefield

We begin with the short-range wakefield for the structure. The small iris aperture of $a/\lambda=0.05$ has the potential for significant short range wake effects. The emittance growth in the structure was analyzed for various beam parameters with variations in offset phase for longitudinal wake suppression and bunch length for transverse wake suppression. The goal was to achieve a residual energy spread in the range of $\sigma_{\delta 0} = 2 \times 10^{-3}$ to 5×10^{-3} and a maximum of 1% correlated energy spread for Balakin-Novokhatski-Smirnov (BNS) damping.

The short-range wakefield study analyzed both the actual cavity profile and an approximate profile, shown in Figure 6 (left), for numerical and analytical calculations, respectively. It was found that the actual and approximate cavity profiles for both the longitudinal loss factor (Figure 6 middle) and transverse loss factor (Figure 7 left) were in close agreement. The resulting longitudinal and transverse wakefield with a $\sigma_z = 150 \mu\text{m}$ are shown in Figure 6 (right) and Figure 7 (right), respectively.

To assess the effectiveness of BNS damping in mitigating the transverse wakefield,²⁴ we make several assumptions. For each linac, we assume an injection energy of 10 GeV with a $\beta_{x0} = 4\text{m}$, and a final energy of 1 TeV with an increase in $\beta \sim E^{1/2}$. Simulations are performed assuming smooth focusing with a 1 nC Gaussian bunch with 51 slices representing $\pm 2.5\sigma_z$. The bunch is offset in normalized coordinates with an initial offset of $x_0 = \sigma_x$. The centroids of all slices for the resulting phase space in x and $\beta x'$ are plotted in Figure 8 with dots for two values of σ_z at $150 \mu\text{m}$ (left) and $100 \mu\text{m}$ (right). The circle shown in Figure 8 gives the amplitude of the initial offset. The correlated energy spread is 1% (tail lower energy than head). The head of the bunch can be identified residing on the circle defined by the initial offset as it does not experience any wakefield. These plots give emittance amplification factor of 4.5 (left case) and 0.76 (right case). We observe that a σ_z of $100 \mu\text{m}$ results in small emittance growth due to an initial transverse offset.

The initial beta-function of $\beta_{x0} = 4\text{m}$ could be provided with a 4-m FODO cell having 90-degrees phase advance. At 10 GeV, this would require 12 cm quadrupoles having a gradient of 200 T/m. To maintain the scaling of the β -function with $E^{1/2}$, the cell and quadrupoles lengths would scale in the same manner and the phase advance would remain 90-degrees²⁵. Achieving the high quadrupole gradient may be most easily achieved with variable strength permanent magnet quadrupoles; a recently constructed device demonstrated 201 T/m with a 10 mm bore and 45% variability²⁶.

To mitigate the longitudinal wakefield, the bunch needs to run off-crest with an average offset in phase. The final offset in phase needs to be determined in conjunction with the correlated energy spread. A calculated residual energy spread of $\sigma_{\delta 0} = 2 \times 10^{-3} / 4.8 \times 10^{-3}$ is achieved with a 21/0 degree average phase offset (ahead of crest) and a modest/negligible 6.5%/0% reduction in gradient.

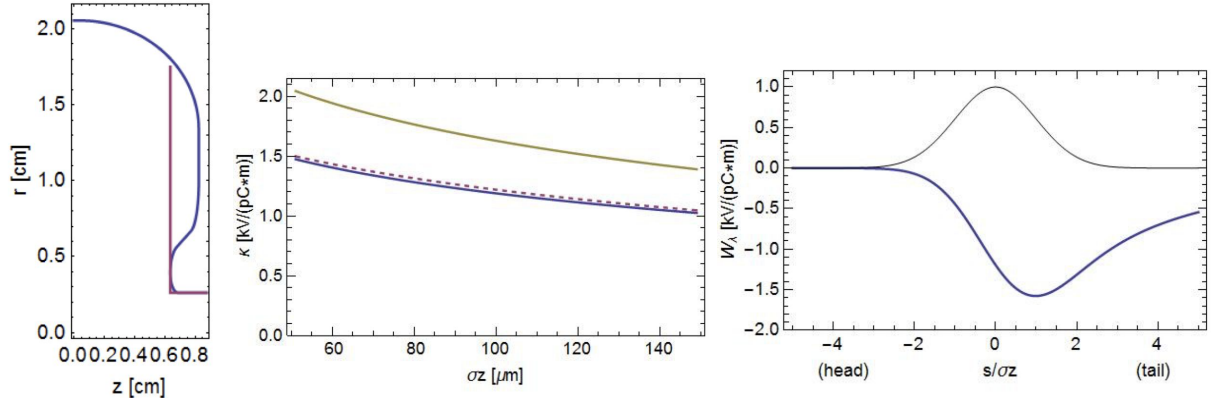


Figure 6 (left) Actual (blue) and approximated (red) structure profile. For the approximated structure a period $p = 1.75$ cm, gap $g = 1.272$ cm, iris radius $a = 0.262$ cm was used. (middle) Longitudinal loss factor (blue), analytical (dashed), alternate π -mode (C-band, $a/\lambda = 0.05$) structure (yellow) vs rms bunch length. (right) Longitudinal bunch wake (blue) and bunch shape (black) with head to left. Result shown for an rms length $\sigma_z = 150$ μ m.

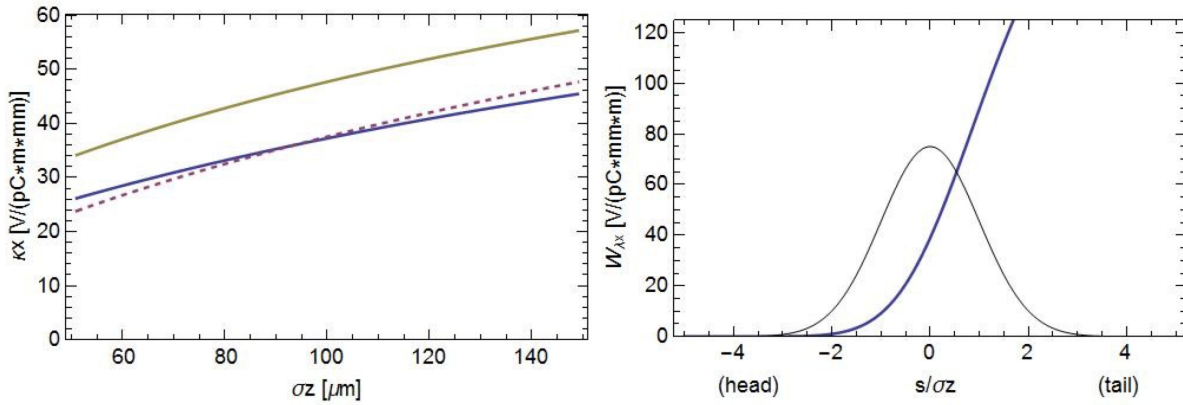


Figure 7 (left) Kick factor (blue), analytical (dashed), alternate π -mode (C-band, $a/\lambda = 0.05$) structure (yellow) vs rms bunch length. (right) Transverse bunch wake (blue) and bunch shape (black) with head to left. Result shown for an rms length rms length $\sigma_z = 150$ μ m.

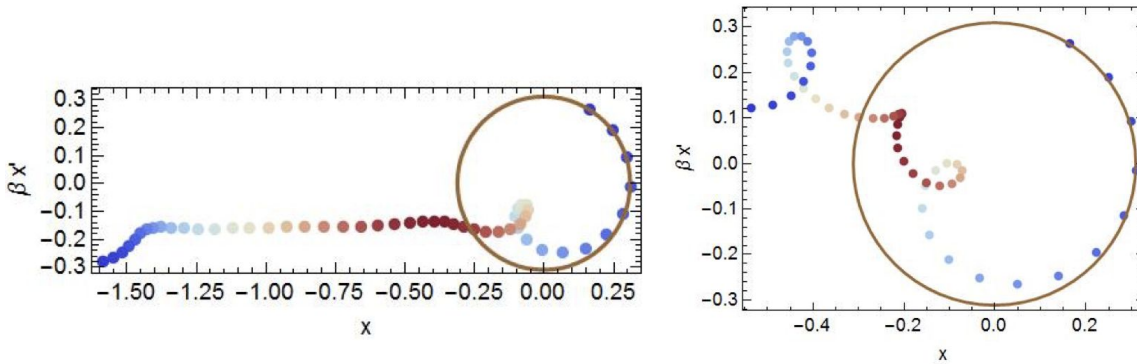


Figure 8 For C-band, $a/\lambda = 0.05$, $2\pi/3$ cavity, 1% BNS correlated energy spread, $\beta_{x0} = 4$ m: $\sigma_z = 150$ μ m (left) and $\sigma_z = 100$ μ m (right). The projected emittance growth factors are 4.5 (left) and 0.76 (right). Slices are color-coded with size of λ_{zi} , where large (small) is red (blue).

b. Long-Range Wakefield

Damping of the long-range wakefield was the subject of extensive investigations for collider design such as NLC and CLIC. Both of these accelerator designs have incorporated cell-to-cell detuning and damping for wakefield suppression²⁷. Detuning works by preventing the coherent addition of dipole modes along the length of the structure. In order to achieve detuning small modifications must be designed and incorporated into each cell of the structure. The modifications require simulation and design with high-performance computing tools that have been developed for linear collider structure design²⁸. The efficacy of detuning is limited by the eventual recoherence of the wakefield modes in the structure and therefore broadband damping must be added to suppress the wakefields. In order to symmetrically suppress both orientations of the dipole mode, structures have been designed with four apertures in each cell that couple to either individually damped waveguides²⁹ containing an absorbing material (SiC) or common manifolds that transport the power away from the structure to a common load³⁰.

Understandably, in the actual structure for the main linac presented in this design, these two well-known means of wakefield suppression will need to be incorporated: 1) by detuning the dipole frequency in a Gaussian density distribution, the wakefield can be dramatically suppressed in a short distance, e.g. at the second bunch of the bunch train; 2) by damping, ideally through the existing manifold and an additional one for the second orientation of the dipole mode, to suppress the wakefield at a longer distance from recoherence of the detuned modes.

The dominant contribution to the long-range dipole wakefield is from the first 2 to 3 dipole passbands of the structure. The contribution of each mode is quantified by the kick factor determined by the structure's geometry. The long-range dipole wakefield, as a function of distance, is calculated as the sum of the sinusoidal spatial oscillations with wavenumbers ω/c , scaled by the kick factors³¹. The dipole wakefield was calculated for a 20-cell C-band structure. The 20 cells are identical and there is no de-tuning incorporated, Figure 9. While the wakefield of such a structure does not represent the final design for a linear collider, the calculation presented here provides a realistic peak value for comparison with other designs.



Figure 9 A 20-cell uniform structure utilized for long-range wakefield calculations.

Figure 10 shows the dipole wakefield for a uniform 20-cell C-band structure. Each cell is $1/3$ of a wavelength. The total structure length is 351 mm. A Q_{damp} of 1000 was used for all the dipole modes. The peak value at the origin is about 50 V/pC/mm/m. This value is about half that of the X-band structure proposed for the NLC. The bunch spacing in consideration is 19 periods of the

C-band wavelength, which is about 1-m. Based on the X-band structure studies for the NLC, about 10% detuning of the dipole modes would be needed to minimize the wakefield at the first subsequent bunch by a factor of >50 , depending on the number of modes used for the detuning. The parallel feeding waveguide, Figure 4 and 5, for the C-band design can naturally provide manifold damping for the dipole modes. Additional damping schemes can be added to achieve the needed damping for both x-y polarizations.

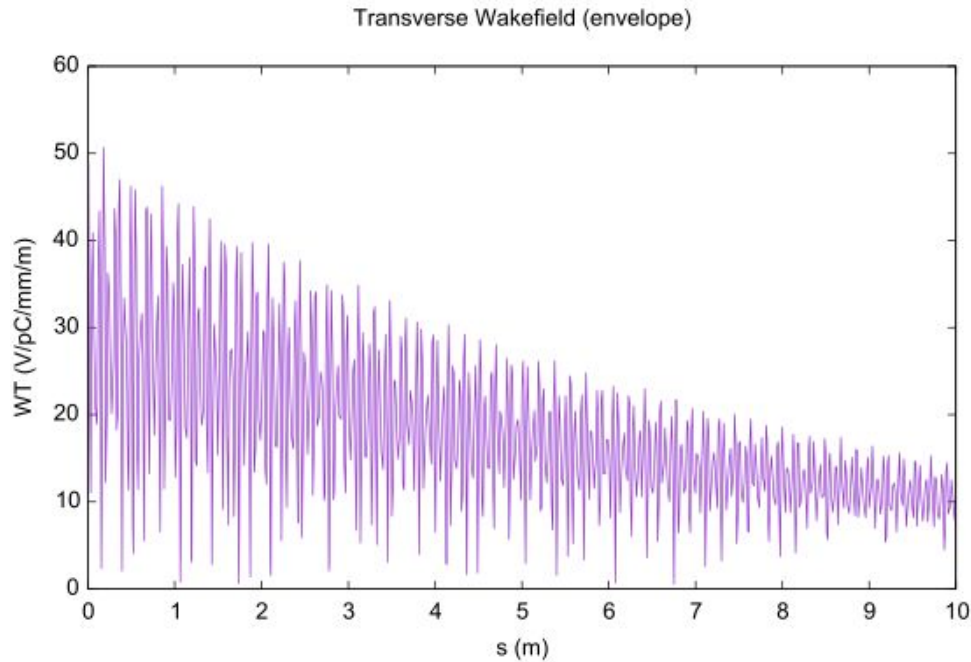


Figure 10 Long-range dipole wakefield for a uniform 20-cell C-band structure.

7. Cryogenic Cooling Complex

The cooling load at cryogenic temperature with the operating parameters assumed in the previous section is 12.2 MW for each 1.0 TeV linac. The linac has a length of ~ 9400 m including a 10% allowance for instrumentation sections, cryogen feeds, etc. The cooling utilizes the latent heat of vaporization of LN of 199 KJ/Kg. The thermal power deposited in the accelerating structures is derived from the difference in RF power and electron beam power, with the parameters given in Table 4. The relative electrical power for the RF and cryogenic cooling system are also listed in the Table.

The simplified cross section of the Cryomodule is shown in Figure 11. The accelerator structure is enclosed in a stainless steel support tube with two-phase flowing nitrogen. LN is supplied from a separate tube and is periodically transversely piped to the accelerator tube. The gas phase is separated from the accelerator and counter-flows back to a nitrogen reliquification plant. These three areas are included within a vacuum insulated steel cryostat. The layout of the reliquification plants is shown in Figure 12.

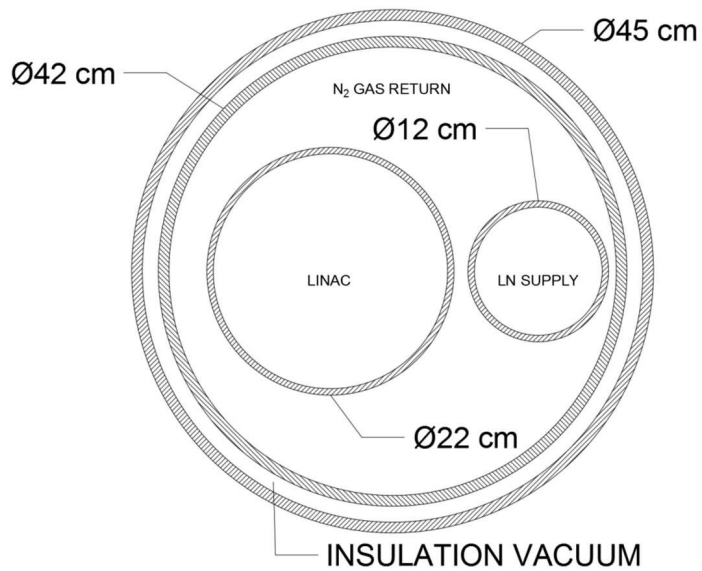


Figure 11 Cross section of a cryomodule.

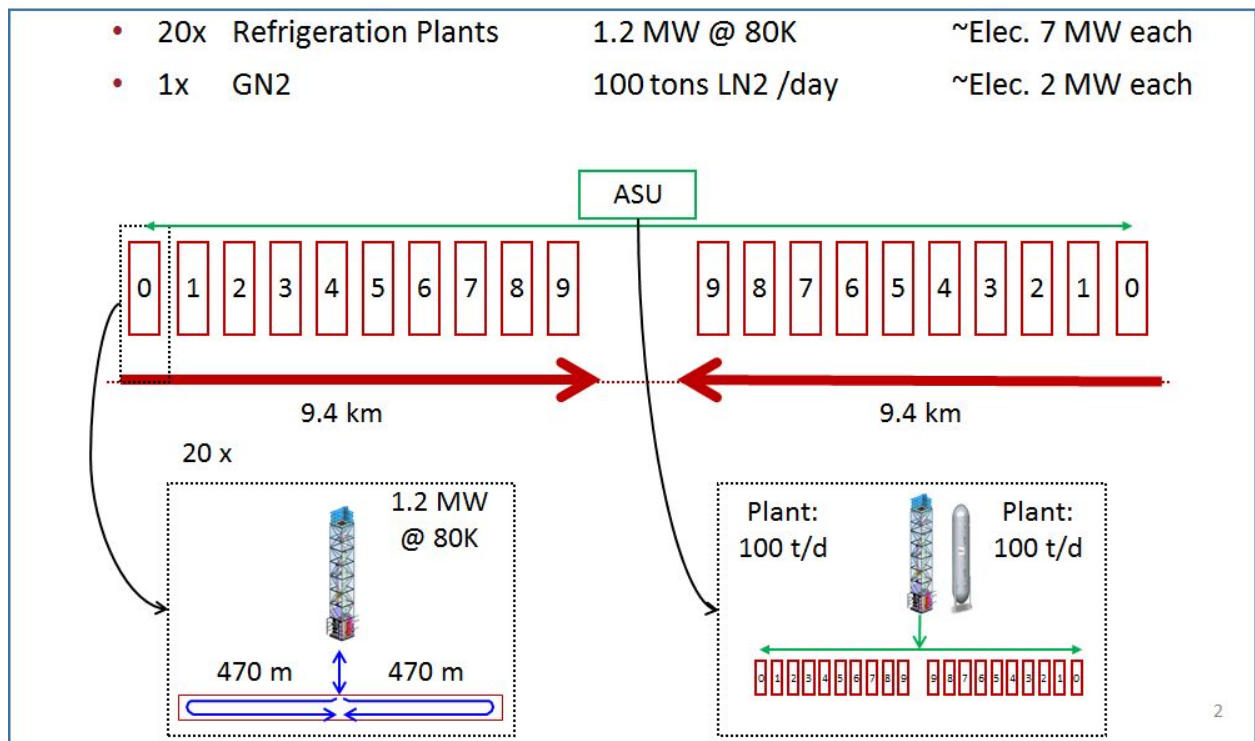


Figure 12 Simplified schematic of the overall cryogenic system.

Each plant has a refrigeration power of 1.2 MW, so each linac requires 10 plants. The LN runs in both directions along the linac, with the length of each run being ~470 m. The power per run is 0.6 MW, and the mass flow of LN into each run is ~3 Kg/s. Using the dimensions in Figure 11, the flow is turbulent with pressure drops (accounting for the flow profile) of 0.09 Bar for the liquid line and 0.09 Bar for the gas line. In addition, an Air Separation Unit (ASU) with a capacity of 100 tonnes/day provides startup and makeup liquid. The linac LN inventory is ~200 m³.

Parameter (2 TeV CoM)	Units	Value
Nitrogen Reliquification Plant Cost for Cryogenic Cooling	M\$/MW	10
Single Beam Power (1 TeV linac)	MW	9
Total Beam Power	MW	18
Total RF Power	MW	42.4
Heat Load at Cryogenic Temperature	MW	24.4
Electrical Power for RF	MW	84.8
Electrical Power for Cryo-Cooler	MW	162.7

Table 4: Parameters at Power Load Required for Cryogenic Cooling Systems

8. Current Experimental Work

X-band distributed coupling accelerator structures using multiple fabrication methods have been built and room temperature tested³² at SLAC with high power RF and with beam³³ at the X-band Test Area in NLCTA³⁴. These experiments have demonstrated the structure's ability to achieve gradients beyond the requirements envisioned here while meeting the designed RF performance. An X-band structure made of hard copper fabricated with e-beam welding has been installed in a LN cryostat and tested with low power RF. The structure's RF performance is shown in Figure 13 at both room temperature and 77K. The intrinsic Q_0 of the structure increased from ~11,000 to 27,500 or an increase of 2.5, which exceeds the assumed increase used for the design presented here. Future measurements will explore the role of material stock and thermal cycling in fabrication (e.g. from brazing) on achieving the largest increase in shunt impedance. The structure and the cryo-vessel will be installed in NLCTA in the next few months for low temperature testing at high gradient.

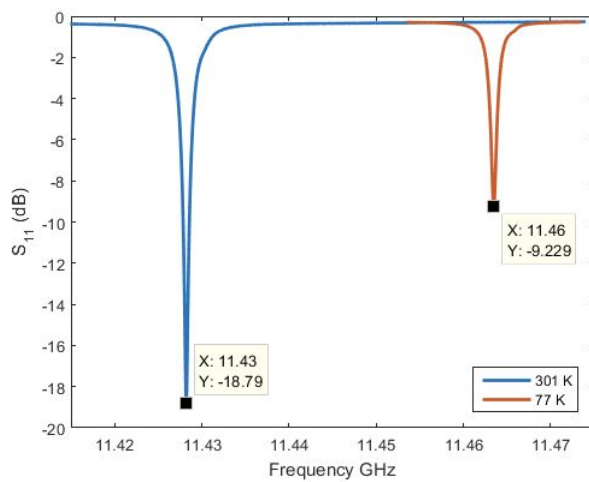


Figure 13 (left) S-parameters measured for an X-band 26 cm distributed coupling structure at both room temperature and 77K. The structure transitioned from being under coupled to overcoupled with a minimum S_{11} of approximately -30 dB observed for critical coupling. (right) Photograph of the cryogenic vessel for an X-band distributed coupling structure. Background grid spacing is one inch.

9. Summary

We have presented a pre-conceptual point design for high gradient, high power linacs aimed at an e^+e^- linear collider in the TeV class. The linac design is based on two features: an accelerator structure with separate feeds to each cavity permitting the iris to be optimized for gradient and breakdown; and a structure that operates in LN, causing the Cu (or Cu alloy) conductivity to increase by about a factor of 2.3. An initial analysis of both short-range and long-range wakefields for the selected parameters is presented. We observe that the short-range wakefield is tolerable with BNS damping and a small average off-crest operation. The long-range wakefield for the basic accelerating structure was found to be slightly less than the NLC design. This indicates that gaussian-detuning and higher-order-mode damping manifolds may address this challenge; however the detailed solution requires further design of the structure and the RF distribution. The optimal gradient for a cost-optimized collider depends strongly on the cost of RF power, and we assume the value from DOE GARD of \$2/peak kW. This RF cost has not yet been demonstrated, but progress is being made on both klystrons and modulators, and will be reported elsewhere. With this RF cost assumption, a 1 TeV linac including tunnels and utilities but not e^+e^- sources, damping rings or bunch compressors would cost ~3G\$, which is significantly less per GeV than other designs.

Acknowledgements

Work supported by the U.S. Department of Energy under contract number DE-AC02-76SF00515.

References

1. ILC Technical Design Report, June 2013, <http://www.linearcollider.org/ILC/Publications/Technical-Design-Report>.
2. Cahill, Alexander, *et al.* "Ultra High Gradient Breakdown Rates in X-Band Cryogenic Normal Conducting Rf Accelerating Cavities." *8th Int. Particle Accelerator Conf.(IPAC'17), Copenhagen, Denmark, 14â 19 May, 2017*. JACOW, Geneva, Switzerland, 2017.
3. "Radiofrequency Accelerator R&D Strategy Report" *DOE HEP General Accelerator R&D RF Research Roadmap Workshop* March 8–9, 2017.
4. ILC values are from The International Linear Collider Machine Staging Report 2017, <https://arxiv.org/abs/1711.00568> Table 5.1; CLIC values are from Updated Baseline for a Staged Compact Linear Collider <https://arxiv.org/abs/1608.07537> Table 9.
5. K. Fujii *et al.*, arXiv:1506.05992 [hep-ex].
6. Fujii *et al.*, arXiv:1710.07621 [hep-ex].
7. CLIC Conceptual Design Report <https://arXiv.org/abs/1202.5940>.
8. H. Abramowicz *et al.*, *Eur. Phys. J. C* **77**, no. 7, 475 (2017) [arXiv:1608.07538 [hep-ex]].
9. T. Barklow, K. Fujii, S. Jung, R. Karl, J. List, T. Ogawa, M. E. Peskin and J. Tian, *Phys. Rev. D* **97**, 053003 (2018) [arXiv:1708.08912 [hep-ph]].
10. Z. Liu, L. T. Wang and H. Zhang, *Chin. Phys. C* **41**, no. 6, 063102 (2017) [arXiv:1612.09284 [hep-ph]].
11. D.M. Asner *et al.*, in *Proceedings of the Community Summer Study on the Future of US Particle Physics* (Snowmass 2013), <http://www.slac.stanford.edu/econf/C1307292/>, arXiv:1310.0763 [hep-ph].
12. T. Barklow, K. Fujii, S. Jung, M. E. Peskin and J. Tian, *Phys. Rev. D* **97**, no. 5, 053004 (2018) [arXiv:1708.09079 [hep-ph]].
13. P. Marquard, A. V. Smirnov, V. A. Smirnov and M. Steinhauser, *Phys. Rev. Lett.* **114**, 142002 (2015) [arXiv:1502.01030 [hep-ph]].
14. M. Low and L. T. Wang, *JHEP* **1408**, 161 (2014)
15. K. Kowalska and E. M. Sessolo, arXiv:1802.04097 [hep-ph].
16. Y. J. Chae and M. Perelstein, *JHEP* **1305**, 138 (2013) [arXiv:1211.4008 [hep-ph]].
17. ILC Technical Design Report <https://arxiv.org/abs/1711.00568> Figure 15.8
18. C. Karzmark, C. Nunan, and E. Tanabe, "Medical electron accelerators," (McGraw-Hill, Incorporated, Health Professions Division, 1993) Chap. 3: Microwave Principles for Linacs.
19. T. Wangler, "Rf linear accelerators," (Wiley, 2008) Chap. 4: Standard Linac Structures.
20. Tantawi, Sami G., Zenghai Li, and Borchard, Philipp, "Distributed coupling and multi-frequency microwave accelerators." U.S. Patent 9,386,682, July 5, 2016
21. M.H. Nasr, S.G. Tantawi, "New Geometrical-Optimization Approach Using Splines for Enhanced Accelerator Cavities' Performance," *IPAC 2018*
22. Table 8-6 <http://www.slac.stanford.edu/accel/nlc/zdr/Snowmass96/ZDRCH08.PDF>
23. <https://cds.cern.ch/record/2157079/files/CLIC%20Note%201066.pdf> for CLIC (2.75 mm <https://clic-meeting.web.cern.ch/clic-meeting/clictable2010.html>)
24. Bane, KARL LF. "Landau damping in the improved SLC linac: A, The sensitivity to injection jitter." No. SLAC/AP-69. Stanford Linear Accelerator Center, Menlo Park, CA (USA), 1988.
25. C. Adolphsen, *et al.*, *Proc IEEE PAC'1995*, 2989 (1995); <https://doi.org/10.1109/PAC.1995.505760>
26. F. Marteau, *et al.*, *Appl. Phys. Lett.* **111**, 253503 (2017); <https://doi.org/10.1063/1.4986856>

27. Li, Z., et al. "Optimization of the X-band Structure for the JLC/NLC." No. SLAC-PUB-11916. 2006.
28. Li, Zenghai, et al. "High-performance computing in accelerating structure design and analysis." *Nuclear Instruments and Methods in Physics Research Section A: Accelerators, Spectrometers, Detectors and Associated Equipment* 558.1 (2006): 168-174.
29. Zha, Hao, et al. "Beam-based measurements of long-range transverse wakefields in the Compact Linear Collider main-linac accelerating structure." *Physical Review Accelerators and Beams* 19.1 (2016): 011001.
30. Jones, Roger M., et al. "Wakefield damping in a pair of X-band accelerators for linear colliders." *Physical Review Special Topics-Accelerators and Beams* 9.10 (2006): 102001.
31. Bane, Karl LF, Perry B. Wilson, and T. Weiland. "Wake fields and wake field acceleration." AIP Conference Proceedings. Vol. 127. No. 1. AIP, 1985.
32. Tantawi et al., "Distributed Coupling Accelerator Structures: A new Paradigm for High Gradient Linacs", Manuscript in preparation.
33. Limborg-Deprey, C., et al. "Performance of a first generation X-band photoelectron rf gun." *Physical Review Accelerators and Beams* 19.5 (2016): 053401.
34. Limborg-Deprey, Cecile, et al. "Commissioning of the X-Band Test Area at SLAC." (2013): MOPB029.